The Astrophysical Journal, 881:127 (13pp), 2019 August 20 https://doi.org/10.3847/1538-4357/ab2cb5

Probing the Gas Content of Late-stage Protoplanetary Disks with N_2H^+

Dana E. Anderson[1], Geoffrey A. Blake[1], Edwin A. Bergin[2], Ke Zhang[2,5], John M. Carpenter[3], Kamber R. Schwarz[2], Jane Huang[4], and Karin I. Öberg[4]

[1] Division of Geological and Planetary Sciences, California Institute of Technology, 1200 E. California Blvd., Pasadena, CA 91125, USA; deanders@caltech.edu
[2] Department of Astronomy, University of Michigan, 1085 South University Ave., Ann Arbor, MI 48109, USA
[3] Joint ALMA Observatory, Av. Alonso de Córdova 3107, Vitacura, Santiago, Chile
[4] Harvard-Smithsonian Center for Astrophysics, 60 Garden St, Cambridge, MA 02138, USA
Received 2018 December 14; revised 2019 June 19; accepted 2019 June 23; published 2019 August 21

Abstract

The lifetime of gas in circumstellar disks is a fundamental quantity that informs our understanding of planet formation. Studying disk gas evolution requires measurements of disk masses around stars of various ages. Because H_2 gas is unobservable under most disk conditions, total disk masses are based on indirect tracers such as sub-mm dust and CO emission. The uncertainty in the relation between these tracers and the disk mass increases as the disk evolves. In a few well-studied disks, CO exhibits depletions of up to 100× below the assumed interstellar value. Thus, additional tracers are required to accurately determine the total gas mass. The relative lack of nitrogen found in solid solar system bodies may indicate that it persists in volatile form, making nitrogen-bearing species more robust tracers of gas in more evolved disks. Here we present Atacama Large Millimeter/submillimeter Array detections of N_2H^+ in two mature, ∼5–11 Myr old disks in the Upper Scorpius OB Association. Such detections imply the presence of H_2-rich gas and sources of ionization, both required for N_2H^+ formation. The Upper Sco disks also show elevated N_2H^+/CO flux ratios when compared to previously observed disks with $\gtrsim$10× higher CO fluxes. Based on line ratio predictions from a grid of thermochemical disk models, a significantly reduced CO/H_2 abundance of $<10^{-6}$ for a gas-to-dust ratio of $\gtrsim$100 is required to produce the observed N_2H^+ fluxes. These systems appear to maintain H_2 gas reservoirs and indicate that carbon- and nitrogen-bearing species follow distinct physical or chemical pathways as disks evolve.

Key words: astrochemistry – molecular data – protoplanetary disks

1. Introduction

The formation of planets in a circumstellar disk is enabled and controlled by the quantity of gas present. Interactions between the gaseous and solid components of the disk play a crucial role in disk dynamics and the initial stages of planet formation (e.g., Weidenschilling & Cuzzi 1993). Following coagulation of micron-sized dust grains into larger particles, the efficiency of further planetesimal growth through streaming instabilities depends on the ratio of gas to solids in the disk (Youdin & Goodman 2005). Gas giant planets are generally thought to form through runaway accretion of disk gas onto sufficiently large planetary cores. The timescales for both the formation and migration of these planets in the disk are limited by the eventual dissipation of disk gas. Furthermore, the exact timing of gas dissipation may determine whether forming-planets become rocky super-Earths or gas giants (e.g., Pollack et al. 1996; Ansdell et al. 2016; Lee & Chiang 2016). The lifetime of disk gas therefore affects both the likelihood of forming of planetary systems and their final architectures. Key components of our theoretical understanding of planet formation depend on estimations of the total disk gas mass over time. Nevertheless, observationally characterizing the gas content of disks of different ages is challenging.

The bulk of disk gas present is expected to be primordial throughout the disk lifetime, inherited from the parent molecular cloud. This gas is removed from the disk as it evolves, first mainly via viscous accretion. Photoevaporation dominates dispersal for the outer radii and for the disk overall at later evolutionary stages, progressing rapidly outward once the inner disk is depleted (Alexander et al. 2014). In this scenario, we would expect to find the last remaining primordial gas in outer regions of the disk. However, the mechanisms for gas dissipation are still largely unconstrained. In particular, the effects of photoevaporation depend on the relative flux of FUV, EUV, and X-ray photons attenuated by disk material (Gorti et al. 2009).

Although gas dissipation itself can be observed directly for the hot disk surface through ion emission (e.g., Pascucci et al. 2011), the evolution of the bulk gas disk must be estimated through measurements of disk masses for systems of different ages. H_2 is the main component of the primordial gas, but does not emit strongly under most disk conditions, resulting in the need for indirect tracers of disk mass. Tracers of inner disk gas include UV continuum excess and H recombination lines, which measure accretion rates; H_2 electronic transitions; and, for radii out to 50 au, *Spitzer* observations of cooling lines at infrared wavelengths (Alexander et al. 2014). Hydrogen deuteride (HD) has also been used as a gas tracer for a small number of disks through *Herschel* measurements (Bergin et al. 2013; McClure et al. 2016), but further use of this tracer is limited by the current lack of instrumentation capable of making these measurements. For older disks and the determination of bulk disk masses, observations of the outer, optically thin regions of the disk are required. Conventional, indirect tracers of the outer disk include (sub-)mm dust continuum and CO isotopologue emission. Estimating the total gas mass of the disk based on these tracers relies on several assumptions, and the validity of these assumptions becomes increasingly questionable with the age of the system as grain growth, gas

[5] Hubble Fellow.

dispersal, and CO depletion invalidate the use of canonical CO/H_2 and dust/H_2 ratios.

Observations of sub-mm continuum from optically thin dust reveal the total disk dust mass in grains of cm size or less. Larger solid bodies are undetectable. Furthermore, dust masses depend on assumptions regarding the dust properties including the opacity. After measuring the dust mass, an assumed gas-to-dust mass ratio is required to estimate the gas mass of the disk. Even if the assumed interstellar value of 100 is valid for disks shortly after formation, this value becomes highly uncertain after several million years of gas and dust evolution. In particular, growth and inward migration of dust may deplete the outer disk of dust particles. Observations of several disks find that the outer edge of the dust disk is interior to that of CO emission, potentially providing evidence of the inward radial drift of solid particles (e.g., Andrews et al. 2012; Zhang et al. 2014).

CO has many advantages as a bulk gas tracer because it is an abundant component of the gas, emissive, and resistant to freezeout (having a condensation temperature of ~20 K). However, the spatial and temporal behavior of the CO/H_2 abundance ratio in the disk is not well understood. A combination of Atacama Large Millimeter/submillimeter Array (ALMA) CO isotopologue and *Herschel* HD measurements reveal CO/H_2 ratios of up to 5–100× below the canonical interstellar value for the three protoplanetary disks with HD detections by *Herschel* (Favre et al. 2013; McClure et al. 2016). Resolved CO isotopologue emission shows depletion of CO even interior to the CO snowline (Schwarz et al. 2016; Zhang et al. 2017). Surveys of nearby star-forming regions also observe lower-than-expected emission from CO isotopologues, indicative of low gas-to-dust ratios and/or widespread CO depletion (Ansdell et al. 2016, 2017; Long et al. 2017). Given the young age of some of these regions, this could indicate that significant CO depletion occurs within 1–3 Myr. Chemical reactions can cause removal of CO from the gas (e.g., Bergin et al. 2014; Reboussin et al. 2015; Yu et al. 2016), but only result in the loss of up to an order of magnitude of CO from the warm molecular layer under the right disk conditions (Schwarz et al. 2018). Physical disk processes are therefore needed to explain further depletion (e.g., Krijt et al. 2018). Without proper evaluation of the CO/H_2 abundance ratio, disk gas masses may be severely underestimated.

Addressing this problem requires additional tracers of the disk gas. Here we investigate another abundant element, nitrogen. Relative to carbon, a smaller fraction of the total available nitrogen abundance (based on the solar value) is found in meteorites and comets (Bergin et al. 2015). The Rosetta mission has revealed a lack of nitrogen in both the volatile ice and refractory phases of comet 67P/Churyumov–Gerasimenko (Rubin et al. 2015; Fray et al. 2017). In fact, comets with high N_2/CO abundance ratios, similar to the estimated value for the solar nebula, are rarely observed (Biver et al. 2018). This may indicate that CO, and perhaps carbon in general, is better captured and/or retained in solid bodies than volatile nitrogen. If not efficiently locked into solid bodies via the planetesimal formation process, the remaining volatile nitrogen may have lingered in the gas phase. Under such conditions, nitrogen-bearing species would be more robust tracers of gas in older, more evolved disks than CO. We aim to investigate this hypothesis.

Nitrogen in the disk is thought to mainly reside in the form of N_2 (Schwarz & Bergin 2014), which has similar volatility to CO (Bisschop et al. 2006; Fayolle et al. 2016), but unfortunately is not emissive under typical disk conditions. However, N_2H^+, a product of N_2 and ionized H_2, is observed in a large number of disks (e.g., Öberg et al. 2010, 2011). Because H_2 is a required precursor and the chemical lifetime of N_2H^+ is relatively short, N_2H^+ detections also indicate the presence of H_2-rich, primordial gas. N_2 has a higher proton affinity than H_2, promoting the generation of N_2H^+ from H_3^+ in ionized H_2 gas. In contrast, abundant N_2H^+ is not expected in gas generated from the destruction of volatile-rich solid bodies because the proton affinity of N_2 is lower than that of H_2O, the major volatile component of comets. This is supported by analysis of the ion chemistry of comet 67P, which reveals that the dominant ion species generated are produced from neutral species with proton affinities higher than that of H_2O (Heritier et al. 2017).

Furthermore, the proton affinity of N_2 relative to that of CO results in the abundances of N_2H^+ and CO being interdependent. In addition to recombination with electrons, proton transfer to CO represents one of the main destruction pathways of N_2H^+, whose abundances and fluxes are therefore sensitive to changes in CO abundance. For this reason, N_2H^+ has been used as a tracer of the CO snowline in protoplanetary disks (e.g., Qi et al. 2013b). Physical/chemical disk models find that both the N_2H^+ column density and emission tend to peak beyond the CO snowline, but the exact location where they peak depends on disk conditions (Aikawa et al. 2015; van 't Hoff et al. 2017). van 't Hoff et al. (2017) identified two regions in the disk where N_2H^+ appears: a layer extending from the midplane beyond the CO snowline and a layer near the disk surface. The surface layer results from N_2 having a slightly lower photodissociation rate than CO when self-shielding by both species is taken into account, and is present when the N_2/CO abundance ratio exceeds 0.2. It appears that both the absolute CO abundance and the N_2/CO ratio are key parameters in determining the N_2H^+ abundance.

Here we use ALMA to search for N_2H^+ emission in two disks in the Upper Scorpious OB Association in order to investigate the use of N_2H^+ as an indicator of disk composition and mass. Disks in Upper Sco are estimated to be ~5–11 Myr old (Preibisch et al. 2002; Pecaut et al. 2012), probing the end of primordial disk evolution and ages around the typical timescale for gas dissipation. Section 2 describes our observations and results including comparison to previous studies. Our grid of thermochemical disk models is introduced and used to interpret our observations in Section 3, and our results are discussed in Section 4. We present our conclusions in Section 5.

2. Observations

2.1. ALMA Cycle 3 Observations

The two disks, J160900–190852 and J160823–193001, were selected based on previous ALMA continuum and CO $J = 3$–2 observations from a Cycle 0 survey of Upper Sco by Carpenter et al. (2014). The disks chosen have readily detectable CO rotational emission, indicating the presence of molecular gas. Both stars are of spectral type K9 and their disks have similar dust masses of 13–14 $M_\oplus$ (Barenfeld et al. 2016). Table 1 describes properties of our selected sources.

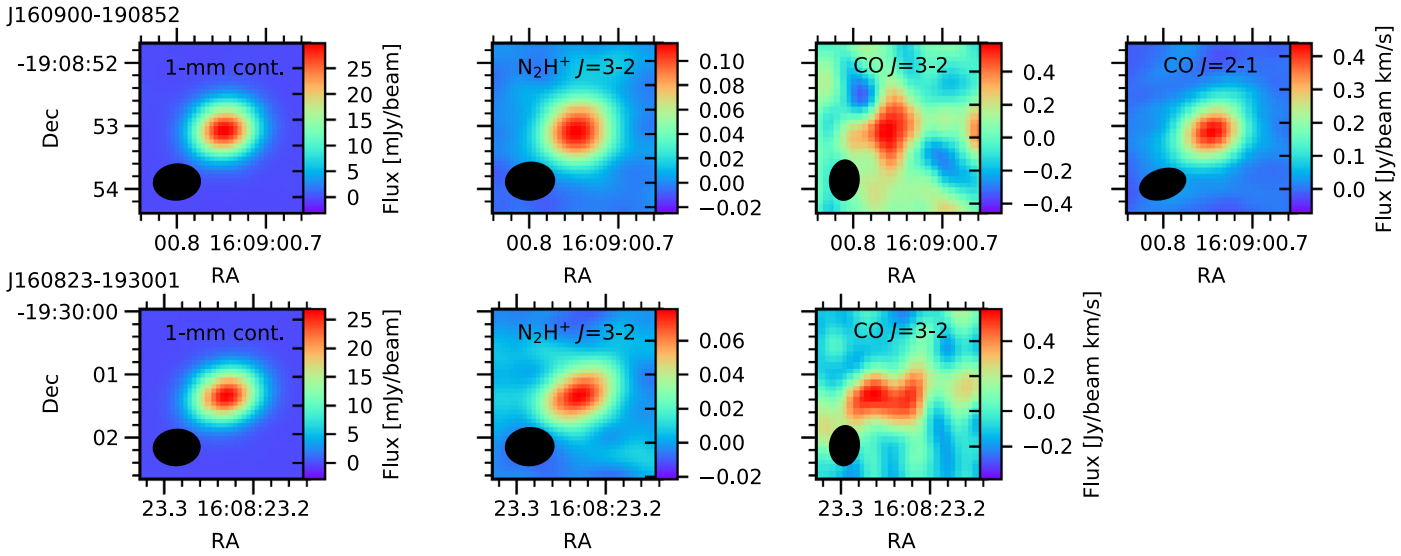

Figure 1. 1.04 mm continuum emission and moment 0 maps of N_2H^+ and CO emission from the Upper Sco disks J160900–190852 (top row) and J160823–193001 (bottom row). Maximum continuum flux values are 26.8 and 29.9 mJy per beam, respectively. The synthesized beam size is indicated in the lower left corner of each subplot.

Table 1
Source Properties

Source	Stellar Properties				Disk Properties	
	Spectral Type	$\log(M_*/M_\odot)$	$\log(L_*/L_\odot)$	$\log(T_*/\mathrm{K})$	Geometry	Dust Mass ($M_\oplus$)[a]
J160900−190852	K9	−0.19(−0.05, +0.05)	−0.45 ± 0.15	3.59 ± 0.01	Full	13.50 ± 3.34
J160823−193001	K9	−0.18(−0.04, +0.05)	−0.59 ± 0.15	3.59 ± 0.01	Full	13.94 ± 3.45

Note.
[a] Barenfeld et al. (2016).

ALMA Band 7 observations (PI: Anderson, 2015.1.01199.S) were taken with the 12 m array during Cycle 3 in 2016 March. Baselines ranged from 15.1 to 460.0 m using 38–41 antennas. The on-source integration time was ∼1.8 hr per source. The desired target was the $N_2H^+ J = 3$–2 line at 279.511 GHz. Five spectral windows were used to capture emission lines each with a bandwidth of 117.19 MHz. These windows were centered at 279.533 GHz for N_2H^+ and 281.549, 282.403, 282.942, and 293.935 GHz for potential additional tracers: H_2CO 4(1,4)–3(1,3), C_3H_2, $D^{13}CO^+$ 4–3, and CS 6–5, respectively. Finally, a window centered at 293.900 GHz with a bandwidth of 1875 MHz was dedicated to the collection of continuum emission.

These measurements are compared with Cycle 3 ALMA observations of J160900–190852 in 2016 June and July (PI: Oberg, 2015.1.00964.S). These data were also collected with the 12 m array, with baselines from 15.1 to 641.5 m in June and to 704.1 m in July. The total time on source was ∼0.35 hr. Spectral windows, each with a total bandwith of 117.19 MHz, were centered at 230.524–230.530, 220.385–220.391, and 219.547–219.553 GHz to capture CO, ^{13}CO, and $C^{18}O$ emission, respectively.

Data calibration was performed using the Common Astronomy Software Applications package (McMullin et al. 2007) version 5.1.2. Atmospheric calibration, bandpass calibration, flux calibration, and phase calibration were applied by the ALMA project. Calibrations were based on observations of J1517–2422 for the bandpass, Titan for the flux, and J1626–2951 and J1553–2422 for the phase for 2015.1.01199.S and J1517–2422 for the bandpass, J1517–2422 in June and Titan in July for the flux, and J1625–2527 for the phase for 2015.1.00964.S. Flux calibration uncertainty is assumed to be 10%. Continuum emission was estimated from line-free channels of all windows and self-calibration was used to produce images using the *clean* algorithm. Spectral line windows were continuum subtracted using *uvcontsub*, then deconvolved using the *tclean* algorithm. We used Briggs weighting with a robust parameter of 1.8, channel widths of 0.5 km s^{-1}, and the "auto-thresh" automasking algorithm with a mask resolution of 0.″25 and mask threshold of 3.0σ. Small mask components identified far from the source location were removed. The resulting mask components were summed over the entire spectral range and the flux within this total masked region was collected for each channel to produce a spectrum. Flux uncertainties listed are based on the rms noise. The rms noise was computed from the standard deviation of the flux measured in 24 different masked regions offset from the source emission combined over all channels containing spectral line emission. The synthesized beam size was approximately 0.″8 by 0.″6 with a position angle of −86° for images from 2015.1.01199.S and 0.″8 by 0.″5 with a position angle of −73° for 2015.1.00964.S.

2.2. Spectral Line Observations

Images and spectra are provided in Figures 1, 2, and 10. Continuum flux densities are derived from the images generated using continuum (line-free) channels with an average frequency of 287.106 GHz (Figure 1). Using the method from Barenfeld et al. (2016), we derived dust masses of 14–15 $M_\oplus$,

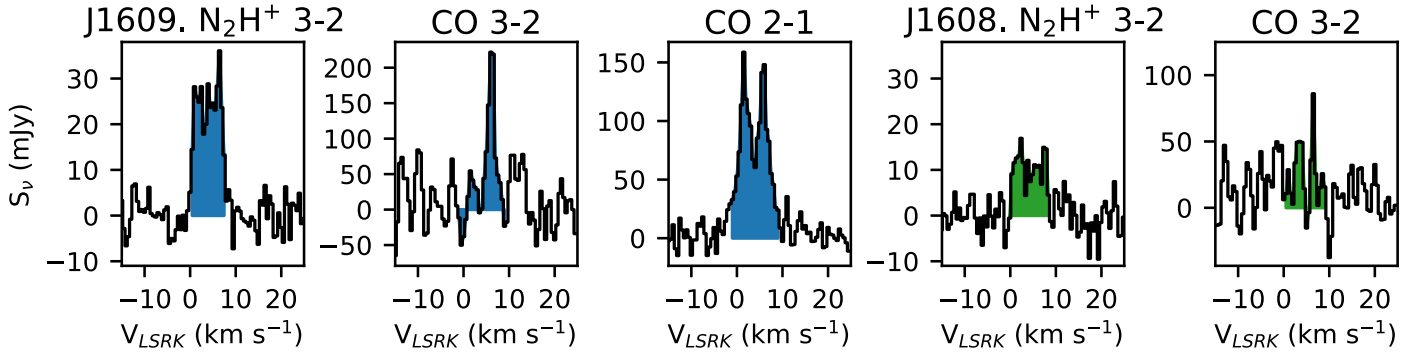

Figure 2. Spectra of N_2H^+ and CO emission from the J160900–190852 (shown in blue) and J160823–193001 (shown in green) disks.

which are consistent with their values from the 0.88 mm continuum.

Spectra were produced as described in Section 2.1 (Figure 2). Summing over the velocity channels containing line emission gave the line fluxes in Table 2. The velocity ranges are 0–7.5 km s^{-1} for N_2H^+ and −1.0–9.0 km s^{-1} for CO $J = 2$–1 in J160900–190852. The CO $J = 2$–1 velocity range is adopted for the CO $J = 3$–2 and $C^{18}O$ $J = 2$–1 emission. These ranges are 0–8.5 km s^{-1} for N_2H^+ and 0.0–9.0 km s^{-1} for CO $J = 3$–2 in J160823–193001. The CO $J = 3$–2 fluxes measured using our method are about 90% of the values found by Barenfeld et al. (2016), 246 ± 42 mJy km s^{-1} J160823–193001, and 815 ± 64 mJy km s^{-1}, for J160900–190852, when a similar velocity range is used (in this case, 1.0–13.5 km s^{-1} for J160900–190852 rather than our narrower range based on the CO $J = 2$–1 emission). Our methods differ in the selection of the aperture, velocity range, and image components used for computing CO fluxes based on the goals of each study. In our further analysis, we elected to use the values derived here using the same method as that for our N_2H^+ measurements to provide an appropriate comparison.

2.3. Comparison to Disks with Strong CO Emission

Figure 3 compares the fluxes observed in our two sources in Upper Sco to observations of other disks where comparable data are available. N_2H^+ has been observed in several bright, gas-rich disks as part of the Disk Imaging Survey of Chemistry with SMA (DISCS) survey with the Submillimeter Array (Öberg et al. 2010, 2011), along with the CO $J = 2$–1 transition. The CO $J = 3$–2 emission from J160823–193001 was scaled using the flux ratio from J160900–190852 (CO $J = 2$–1/CO $J = 3$–2 flux ∼1.9) to produce the CO $J = 2$–1 estimate used in Figure 3. This scaling ratio could be the result of low excitation temperatures similar to those derived for Taurus disks (e.g., Guilloteau et al. 2016) and would be lower, ∼0.3, for the case of optically thin gas in local thermal equilibrium (LTE) at 20 K. Additional disks have been observed by the SMA and/or ALMA including TW Hya, HD 163296, and V4046 Sgr (Rosenfeld et al. 2012, 2013; Qi et al. 2013a, 2015; Kastner et al. 2018). In comparison to the Upper Sco disks, the other disks have CO fluxes typically 1–2 orders of magnitude higher (Figure 3, top panel). However, the N_2H^+ $J = 3$–2 fluxes, some of which are upper limits, are at most an order of magnitude higher than the Upper Sco values. This results in relatively high N_2H^+/CO flux ratios in Upper Sco compared to the other disks (Figure 3, middle panel).

$C^{18}O$ $J = 2$–1 data are available for a selection of the sources including the Upper Sco disk J160900–190852 (PI: Öberg, 2015.1.00964.S). $C^{18}O$ is a more accurate tracer of the disk material given that it has relatively optically thin emission as compared to the more abundant and optically thick $^{12}C^{16}O$ parent isotopologue. The $N_2H^+/C^{18}O$ flux ratio therefore provides a closer approximation of the relative abundances. $C^{18}O$ fluxes are taken from the literature for TW Hya (Qi et al. 2013b), HD 163296 (Qi et al. 2015), IM Lup (Cleeves et al. 2016), AS 209 (Huang et al. 2016), and V4046 Sgr (Kastner et al. 2018). The values for LkCa 15 and MWC 480 were estimated from moment 0 maps prepared as part of the study by Huang et al. (2017). An upper limit of the $C^{18}O$ flux in J160900–190852 is estimated as 3× the rms flux collected using the CO $J = 2$–1 masked region and velocity range (described in Sections 2.1–2.2). This upper limit on $C^{18}O$ provides a lower limit for the $N_2H^+/C^{18}O$ ratio, which is above the values for the other observed disks (Figure 3, bottom panel). This reinforces the trend seen in the N_2H^+/CO values.

Table 2
Observed Line Fluxes

Continuum	Line Flux (mJy km s^{-1})			
1.04 mm	N_2H^+	CO	CO	$C^{18}O$
(mJy)	$J = 3$–2	3–2	2–1	2–1
J160900−190852				
36.4 ± 0.3	183 ± 8	460 ± 68	860 ± 21	43 ± 17
J160823−193001				
32.4 ± 0.4	90 ± 7	222 ± 39	…	…

3. Modeling

3.1. Thermochemical Disk Models

In the following sections, we aim to explore the general trends in N_2H^+ and CO fluxes for disks of varying gas mass and composition. The thermochemical and radiative transfer code of Du & Bergin (2014) is used to run a set of disk models in order to estimate spectral line ratios for the various cases. Initial parameters for the fiducial model are included in Table 3. The parameters describing the central star are set based on Barenfeld et al. (2016) for the two Upper Sco sources observed here and the stellar spectrum of the well-studied T Tauri star TW Hya is used. The disk outer radius is set at 100 au (the effects of this choice are explored in Section 3.3). Gas and dust components share a mass surface density profile with an exponent of 1.0 and an initial scale height of 10 au at a radius of 80 au. Vertical structure is determined using hydrostatic equilibrium over multiple iterations of the dust temperature calculation with a Monte Carlo radiative transfer model. The dust contains two components with sizes following a Mathis–Rumpl–Nordsieck (MRN) distribution: 90% of the dust mass is

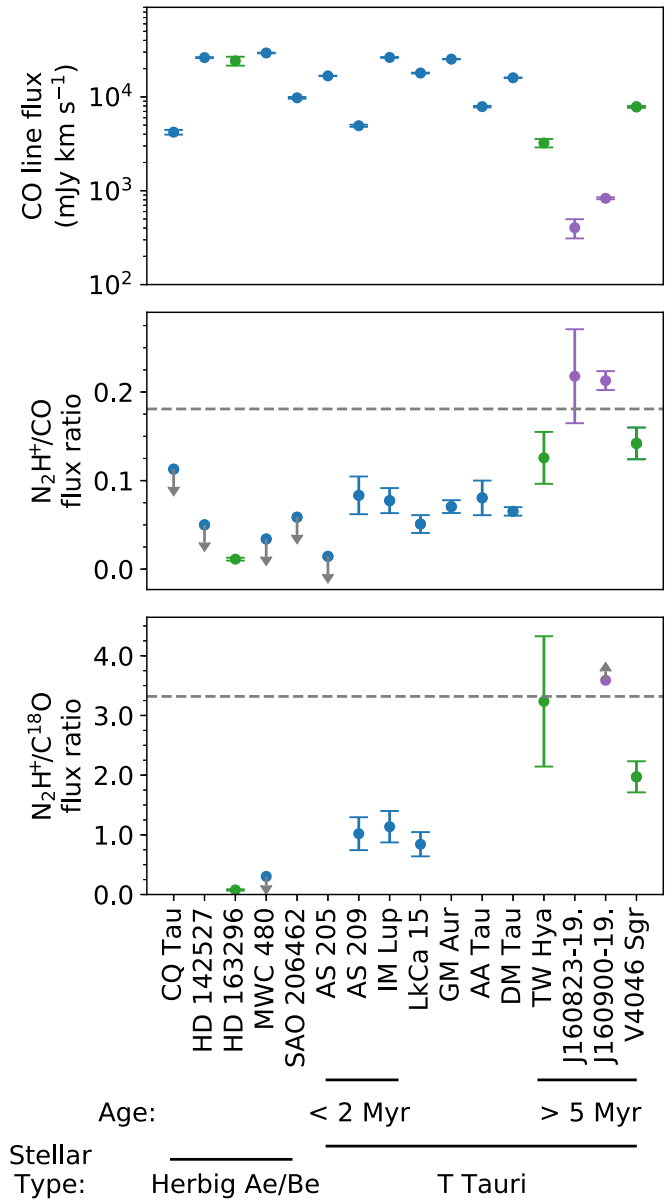

Figure 3. Comparison of CO $J = 2$–1 line fluxes (scaled to a distance of 140 pc based on Gaia Collaboration et al. (2018), top panel), N_2H^+ $J = 3$–2/CO $J = 2$–1 flux ratios (middle panel), and N_2H^+ $J = 3$–2/$C^{18}O$ $J = 2$–1 flux ratios (bottom panel) among disks where data were obtained. This includes 11 disks from the DISCS survey with the Submillimeter Array (Öberg et al. 2010, 2011, indicated in blue), V4046 Sgr (Kastner et al. 2018), and HD 163296 (Rosenfeld et al. 2013; Qi et al. 2015) from ALMA (indicated in green), TW Hya (Rosenfeld et al. 2012; Qi et al. 2013a) from the SMA and ALMA (also indicated in green), and 2 disks in Upper Sco from ALMA (this work, indicated in violet). The dashed line indicates 3 standard deviations above the mean for all sources excluding Upper Sco. Arrows indicate upper or lower limits. $C^{18}O$ values are included when available (PI: Öberg, 2013.1.00226.S & 2015.1.00964.S; Qi et al. 2013b, 2015; Cleeves et al. 2016; Huang et al. 2016; Kastner et al. 2018). The 3σ upper limit of the $C^{18}O$ $J = 2$–1 flux is used to derive the J160900–190852 $N_2H^+/C^{18}O$ limit.

in large dust grains, up to 1 mm in radius, and the remaining in small dust, up to 1 μm in radius. The surface density of the large dust is tapered in the outer disk beyond 60 au as follows: $\Sigma'(r) = \Sigma(r)\exp((r - r_{\rm out})/r_s)$, if $r > r_{\rm out}$, where $r_{\rm out}$ is 60 au and r_s is 5 au. The mass of the gas disk for the fiducial model is 4×10^{-3} $M_\odot$, based on a total dust mass of 4×10^{-5} $M_\odot$ or 13–14 $M_\oplus$ from Barenfeld et al. (2016) and a gas-to-dust mass ratio of 100. The chemistry and disk temperature are evolved for 10^6 yr.

Table 3
Fiducial Model Input Parameters

Stellar Properties:	
M_*	0.65 $M_\odot$
R_*	1.25 $R_\odot$
T_*	3890 K
Source of stellar spectrum	TW Hya
$L_{\rm X\text{-}ray}$	1.6(30) erg s^{-1}
Disk Properties:	
Disk gas mass	4(−3) $M_\odot$
Disk dust mass	4(−5) $M_\odot$
Inner radius	1 au
Outer radius	100 au
Scale height at radius of 80 au	10 au
Power index: surface density versus radius	1.0
Power index: scale height versus radius	1.0
Total run time	10^6 yr
Turbulent viscosity	$\alpha = 0.01$
H_2 cosmic-ray ionization rate	1.36(−17) s^{-1}
Initial abundances: (Relative to total H)	
H_2	5.0(−1)
He	9.0(−2)
CO	1.4(−4)
N	7.5(−5)
H_2O ice	1.8(−4)
S	8.0(−8)
Si^+	8.0(−9)
Na^+	2.0(−8)
Mg^+	7.0(−9)
Fe^+	3.0(−9)
P^+	3.0(−9)
F^+	2.0(−8)
Cl^+	4.0(−9)

Note: a(b) indicates a $\times$ 10^b.

The initial composition of the gas is based on interstellar values. All volatile carbon is assumed to be in the form of gas-phase CO at an abundance of 1.4×10^{-4} relative to total H. Nitrogen starts in the form of gas-phase N at an abundance of 7.5×10^{-5}. The binding energies assumed for pure ices of CO and N_2 are 855 and 800 K, respectively (Bisschop et al. 2006). CO self-shielding is included in the model and we added self-shielding of N_2. N_2 shielding as a function of H, H_2, and N_2 column densities is determined by Heays et al. (2014).

We test the effects of two types of changes to the disk gas: (1) selective depletion of the initial CO gas abundance, and (2) a decrease in the total gas abundance where the relative abundances of chemical species remain at their initial interstellar values. We therefore run seven models including the fiducial model; models with initial CO abundances reduced by factors of 10×, 100×, and 1000×; and with total gas masses reduced by factors of 10×, 100×, and 1000×. In the models with initial CO depletion, the N and all other initial abundances are held constant at the fiducial levels. When the gas mass is reduced, the dust-to-gas mass ratio in the model is increased proportionally. Additional modeling described in Section 3.3 explores the effects of varying the disk temperature, nitrogen content, ionization, size, dust scale height, and lifetime. For a full list of models tested see Table 4.

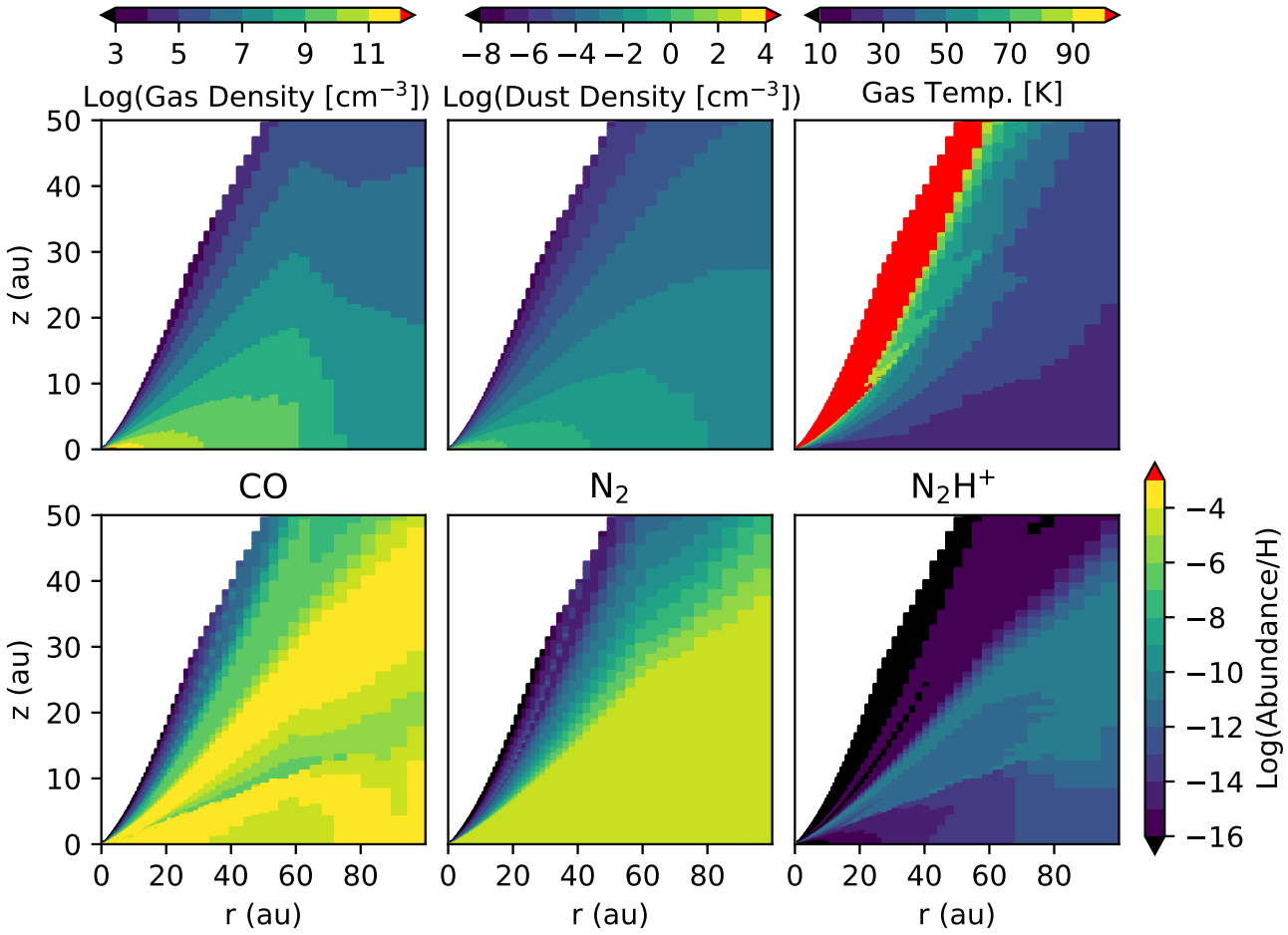

Figure 4. Disk gas density, dust density, gas temperature, and abundances of CO, N_2, and N_2H^+ after 1 Myr in our fiducial model.

Table 4
Model Variations

Model	Varied Parameters	Values
Fiducial with CO depletion	Initial CO abundance	1.4(−5), 1.4(−6), 1.4(−7) per total H
Fiducial with low mass	Disk mass	4(−4), 4(−5), 4(−6) $M_\odot$
	Gas-to-dust mass ratio	10, 1, 0.1
Low mass disk with high N	Initial N abundance	7.5(−4), 7.5(−2) per total H
	Disk mass	4(−6) $M_\odot$
	Gas-to-dust mass ratio	0.1
Low mass disk with high ionization	Cosmic-ray ionization rate	3(−16), 3(−14) s^{-1}
	Disk mass	4(−6) $M_\odot$
	Gas-to-dust mass ratio	0.1
Low mass disk with high stellar ionization	Stellar X-ray luminosity	1.6(32) s^{-1}
	Disk mass	4(−6) $M_\odot$
	Gas-to-dust mass ratio	0.1
Fiducial with low ionization	Cosmic-ray ionization rate	3(−19) s^{-1}
Smaller fiducial	Outer radius	50 au
Larger fiducial	Outer radius	200 au
Larger fiducial with high mass	Outer radius	200 au
	Disk mass	5(−2) $M_\odot$
	Gas-to-dust mass ratio	100
Cold disk	Scale height of large and small grain populations at $r = 80$ au	5 au
	Determination of vertical disk structure	Fixed
	*All variations above were also tested with this disk structure	Also included disk mass of 4(−2)$M_\odot$ Gas-to-dust mass ratio of 1000
Settled disk (large dust)	Scale height of large grain population at $r = 80$ au	1, 2, 5, 10 au
	Determination of vertical disk structure	Fixed

Note: a(b) indicates a × 10^b.

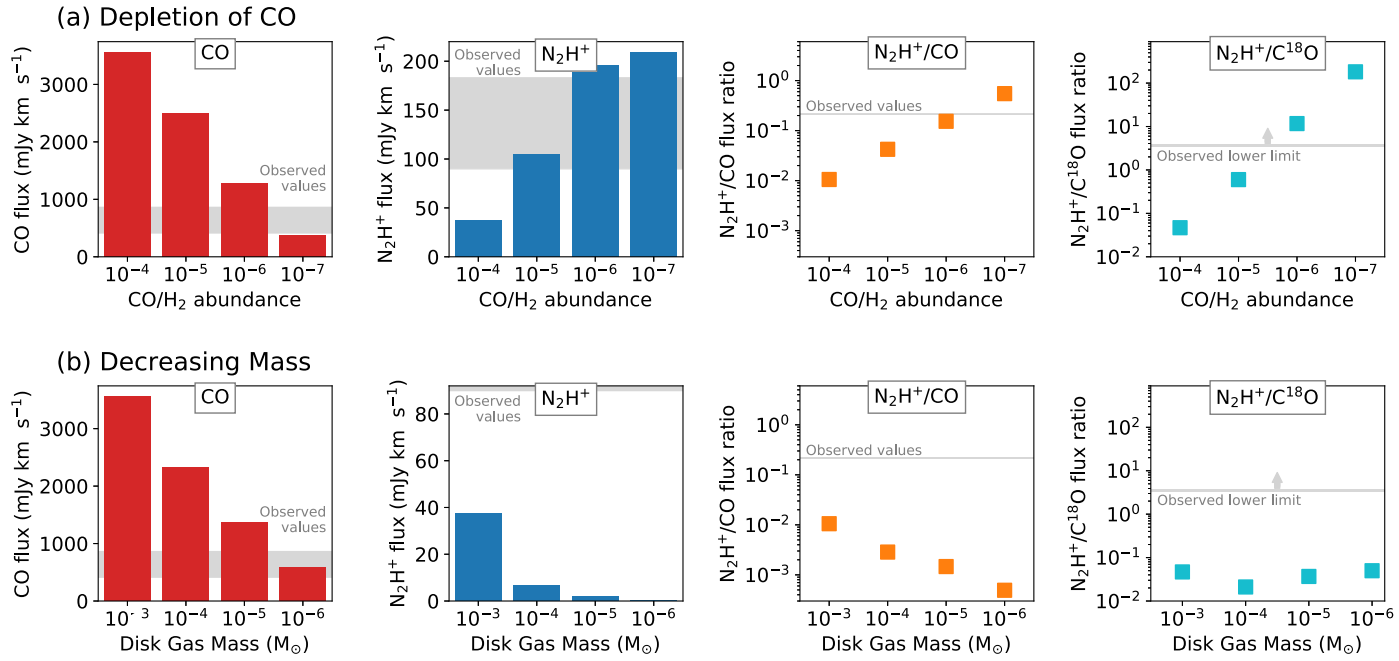

Figure 5. Calculated fluxes for our set of disk models. From left to right, the CO $J = 2$–1 flux, N_2H^+ $J = 3$–2 flux, ratio of the N_2H^+ $J = 3$–2 to CO $J = 2$–1 flux, and ratio of the N_2H^+ $J = 3$–2 to $C^{18}O$ $J = 2$–1 flux are plotted. Values are shown for the fiducial model and additional models where the CO/H_2 abundance ratio is lowered by factors of 10–1000× (a), and for the fiducial model and additional models where the disk gas mass is lowered by factors of 10–1000× (b). The range of observed values for the Upper Sco sources are show for comparison in gray.

3.2. Modeling of Line Ratios

As described in Section 3.1, the thermochemical disk models (Du & Bergin 2014) simulate a low mass, 13 $M_\oplus$, dust disk around a star similar to our Upper Sco sources for various disk gas masses and CO/H_2 abundance ratios. Figure 4 shows the disk gas and dust densities and resulting temperature and abundance distributions for CO, N_2, and N_2H^+ after 10^6 yr for the fiducial model.

The model setup assumes an outer disk radius of 100 au and an inclination of 45° at a distance of 140 pc. Figure 5 shows the calculated line fluxes for CO $J = 2$–1 and N_2H^+ $J = 3$–2 in addition to ratios of the N_2H^+/CO and $N_2H^+/C^{18}O$ fluxes for various disk models in comparison to the observed values. $C^{18}O$ abundances are based on an assumed interstellar $^{18}O/^{16}O$ ratio of 0.002 relative to CO. Actual values may be up to 10× lower than simulated due to isotopic processes in the disk that were not included in our model (Visser et al. 2009; Miotello et al. 2014) producing lower $C^{18}O$ fluxes.

Our thermochemical models reveal distinct trends in spectral line ratios. CO and $C^{18}O$ fluxes decrease with both the CO/H_2 abundance ratio (Figure 5(a), CO shown in red bars) and disk gas mass (Figure 5(b)). However, whereas N_2H^+ fluxes also decrease with decreasing disk gas mass (Figure 5(b), shown in blue bars), they display the opposite behavior with regard to CO depletion (Figure 5(a)). As the CO/H_2 ratio decreases, the N_2H^+/CO flux ratio increases significantly (Figure 5(a), shown in orange points). The increase in N_2H^+/CO is expected based on theoretical predictions of chemistry in such environments. It is not only due to the increase in relative N_2/CO abundances but also because when CO is abundant, it actively destroys N_2H^+ (Qi et al. 2013b, see Section 1). The $N_2H^+/C^{18}O$ flux ratios reinforce the trend with CO abundance (Figure 5(a), shown in light blue points). In comparison, decreasing the disk mass causes the N_2H^+/CO flux ratio to decrease to levels well below the observed values (Figure 5(b), shown in orange points). Rather than decreasing, the $N_2H^+/C^{18}O$ flux ratios appear to remain roughly constant with

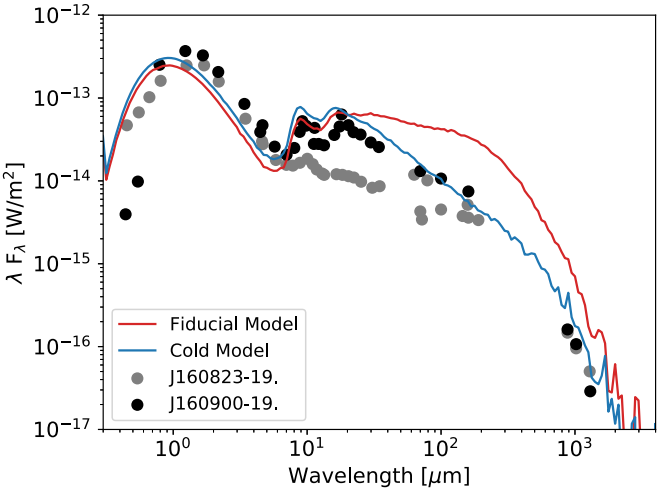

Figure 6. Modeled SEDs for fiducial (red line) and cold disk (blue line) models used in this work. SED data points are taken from the literature (Mathews et al. 2013, and data within).

decreasing disk mass (Figure 5(b), shown in light blue points). This difference is caused by the relative optical depth of the species' emission. Modeled outer disk column densities of N_2H^+ and $C^{18}O$ indicate that the emission from these species is optically thin (or close to optically thin in the case of $C^{18}O$ for CO at interstellar abundances) and therefore traces the disk mass. When CO is abundant, its emission is optically thick, limiting its response to the decreasing disk mass.

Low CO fluxes can be achieved by either low CO abundances or low disk gas masses, but recreating the observed N_2H^+/CO values in Upper Sco requires sufficient H_2 gas in combination with CO depletion. According to the model grid shown in Figure 5, CO depletion by 100–1000× relative to the interstellar abundance is required to reproduce the N_2H^+/CO

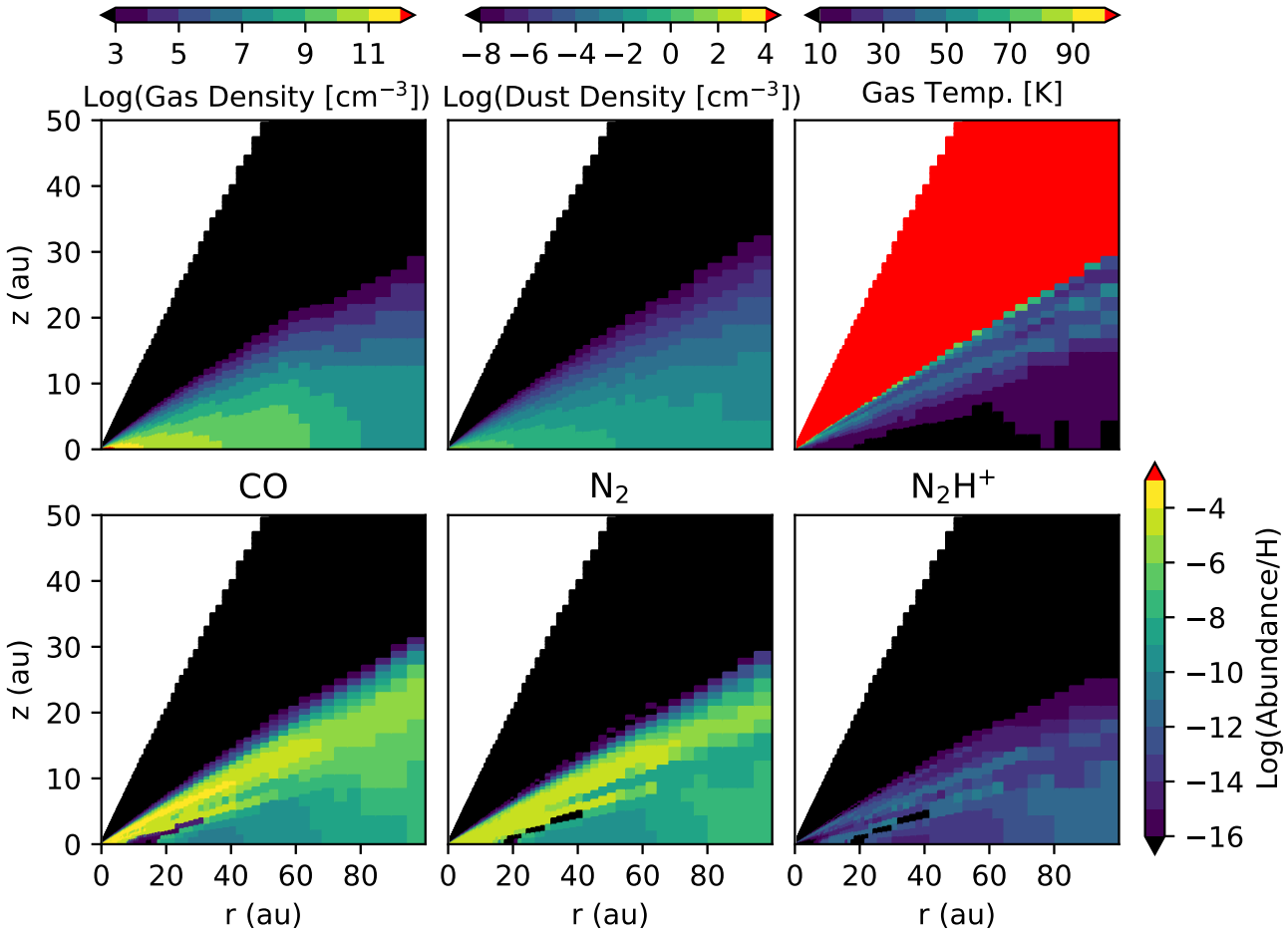

Figure 7. Disk gas density, dust density, gas temperature, and abundances of CO, N_2, and N_2H^+ after 1 Myr in our cold disk model.

flux ratios seen in J160823–193001 and J160900–190852. Similar CO depletion is also needed to exceed the lower limit of the $N_2H^+/C^{18}O$ flux ratio estimated for J160900–190852.

3.3. Alternative Scenarios

The N_2H^+/CO flux ratio will be sensitive to various physical and chemical parameters. The disk temperature structure, for example, will affect the location of CO and N_2 snowlines and determine the emitting regions of each species, while the initial abundances of N and C further set the observed flux ratios. The formation of N_2H^+ is also affected by the level of ionization in the disk. In this section, we aim to test whether or not these and other factors alter our main result that, given our disk model, gas-rich disks with CO/H_2 substantially below the interstellar value are needed to explain high N_2H^+/CO flux ratios, such as those observed in the Upper Sco disks. First, we compare two different sets of physical disk models, the fiducial setup presented in the previous section and a colder disk model, produced by enhanced grain settling. Next we evaluate two other possible explanations of the observed N_2H^+/CO flux ratios: enhanced N/C elemental abundances and enhanced disk ionization rates. Then we discuss the effects of disk size, the degree of dust settling, and the disk lifetime.

3.3.1. Spatial Origin of N_2H^+ Emission

The cold models differ from the previous model set by using a fixed vertical disk structure with the scale height of both the large and small dust set to 5 au at a radius of 80 au, rather than the hydrostatically supported disk. Compared to the fiducial model, which overproduces continuum emission in the far-infrared, the cold disk better approximates the observed spectral energy distributions (SEDs; Figure 6). Reducing the vertical extent of the small dust population together with the large dust prevents mid-infrared fluxes from exceeding those observed. The cold disk structure and relevant chemical abundances are shown in Figure 7.

In a sufficiently cold disk, CO freezeout allows N_2H^+ to form in abundance beyond the CO snowline as long as sufficient N_2 is present. N_2H^+ also originates from the surface layers, sensitive to the N_2/CO ratio as a result of self-shielding by both molecular species and the fact that N_2 has a slightly lower photodissociation rate (van 't Hoff et al. 2017). This N_2H^+ surface layer exists for the less-settled fiducial disk models producing N_2H^+ emission even when the disk is too warm to have a CO snowline. The degree of settling in the cold disk models causes this surface layer to largely disappear. However, the temperatures in the cold disk model are also low enough to produce a CO snowline. These regions are consistent with the emerging interpretation of radial patterns of CO and N_2H^+ in disks (van 't Hoff et al. 2017). The location of the CO snow surface relative to the distribution of N_2H^+ in a selection of our models is shown in Figure 8. Ultimately, our model comparison shows that regardless of whether N_2H^+ originates from a limited region beyond the CO snowline (in the cold disk) or the surface layers of the disk (in the fiducial disk), the trends in the N_2H^+/CO and $N_2H^+/C^{18}O$ flux ratios are the

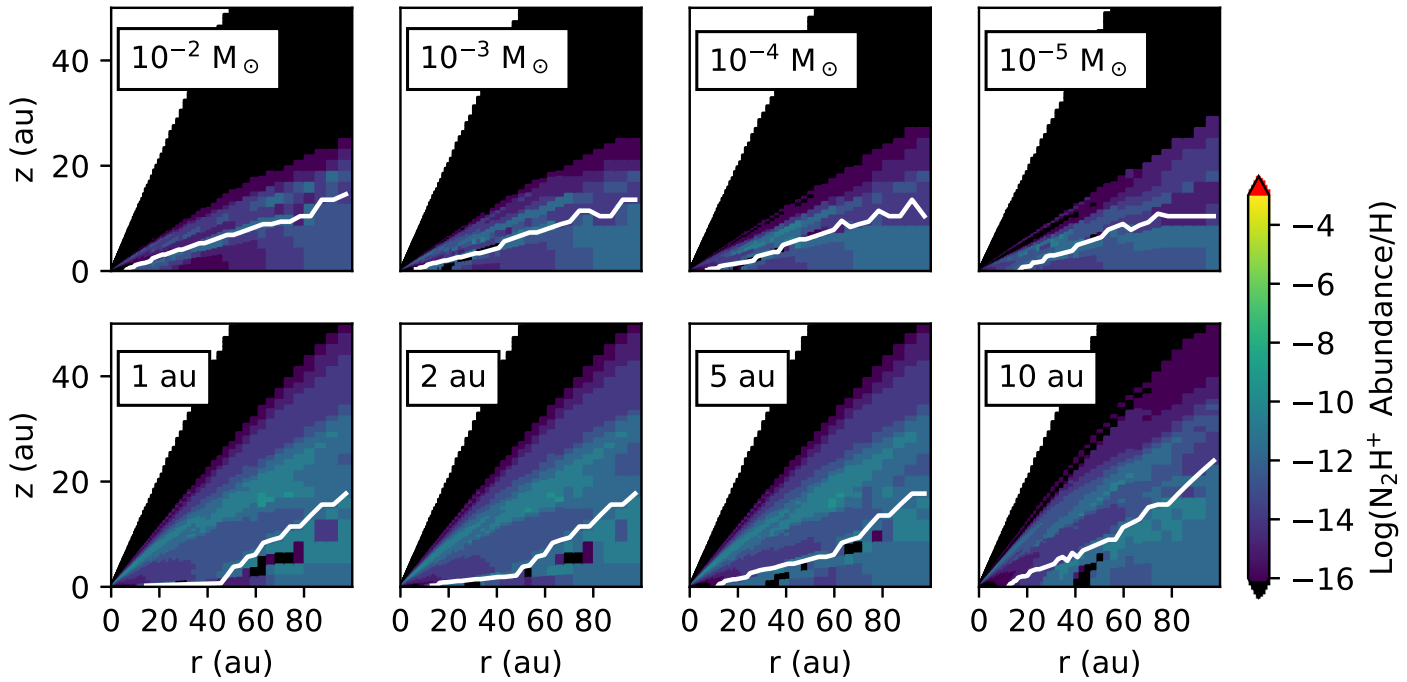

Figure 8. Location of the CO snow surface (indicated by the solid white line) plotted on top of the N_2H^+ abundance distribution in a subset of the disk models. The unsettled models based on the fiducial disk setup are too warm for a CO snowline to be present within 100 au with the exception of the high mass (10^{-2} $M_\odot$) disk models. This set of models is therefore not plotted. The CO snow surface location changes with the disk mass in the cold disk models (upper row). Furthermore, the degree of settling of the large dust relative to the fiducial model also affects the CO snow surface location (lower row). Panels are labeled in the top lefthand corner with the disk mass (upper row) or the scale height of the large dust at 80 au (lower row).

same (Figures 5 and 9). These ratios increase as CO is selectively depleted and remain roughly constant or decrease with decreasing total gas content.

Whereas the cold models better approximate the SEDs, the models based on the fiducial setup provide higher line fluxes, which are needed to reproduce the N_2H^+ observations in the Upper Sco disks. Assuming a gas-to-dust mass ratio of 100, CO/H_2 depletion by 100–1000× is required to reach the observed N_2H^+/CO flux ratios. However, the absolute N_2H^+ and CO fluxes are underproduced for the cold disk conditions. Even after increasing the disk H_2 mass by a factor of 10, the predicted N_2H^+ flux is only 63 mJy km s^{-1} and CO is 260 mJy km s^{-1} for a CO/H_2 abundance of 10^{-7}. These values could further increase if the elemental N/C ratio and/or ionization rates in the disk are enhanced relative to our model assumptions. A complete exploration of this parameter space will be performed in future work.

3.3.2. Enhanced N/C and Disk Ionization

Without any CO depletion, achieving CO fluxes below 1000 mJy km s^{-1} requires gas-to-dust mass ratios 1000× below interstellar in the fiducial model. We therefore ran test models with a gas-to-dust ratio of 0.1 (gas mass of 4×10^{-6} $M_\odot$) to approximate the low CO flux observed in the Upper Sco disks for three additional scenarios: (1) increased initial N abundances of 7.5×10^{-4}–7.5×10^{-2} relative to H, 10–1000× higher than the original model, (2) an increased cosmic-ray ionization rate of 3×10^{-16} s^{-1}–3×10^{-14} s^{-1}, 1–3 orders of magnitude above the interstellar value used in the original model, and (3) a stellar X-ray luminosity of 1.6×10^{32} erg s^{-1}, the maximum value associated with T Tauri stars (see Table 4). All three sets of changes produced higher N_2H^+ fluxes. Increasing the nitrogen content of the disk increased the N_2H^+ flux by a factor of ∼4 for N/H = 7.5×10^{-4} and ∼6 for N/H = 7.5×10^{-2} relative to the original 0.1 gas-to-dust ratio model. However, the N_2H^+/CO flux ratios of 0.002–0.003 and $N_2H^+/C^{18}O$ flux ratios of 0.17–0.25 remain too low to reproduce the observed Upper Sco values even when considering rather extreme nitrogen abundances. The same is true for the cold disk models with gas-to-dust ratios of 10–100.

Increasing the comic-ray ionization rates had a greater effect on the targeted flux ratios by enhancing the N_2H^+ flux while simultaneously decreasing the CO and $C^{18}O$ fluxes. N_2H^+/CO flux ratios increased to 0.01 for an ionization rate of 3×10^{-16} s^{-1} and 0.2 for 3×10^{-14} s^{-1} relative to the fiducial model. This is approaching the observed values in Upper Sco. The $N_2H^+/C^{18}O$ flux ratios were much greater, with values of 5–90. The cold disk models saw similar increases with a maximum of 0.08 and 13 for N_2H^+/CO and $N_2H^+/C^{18}O$, respectively, for an ionization rate of 3×10^{-14} s^{-1}. Nevertheless, the individual fluxes of N_2H^+ and CO were lower than in the previous gas-rich models with similar flux ratios. For the model with 1000× the interstellar cosmic-ray ionization rate and an N_2H^+/CO flux ratio at the lower end of the observed Upper Sco values, the N_2H^+ and CO fluxes were at least a factor of ∼3 below those observed in the weaker of the two Upper Sco disks. The cosmic-ray ionization rate is not well constrained in disks, but current observations of TW Hya suggest that the rate in this disk is low, less than 10^{-19} s^{-1} (Cleeves et al. 2015). Rates this low produce fluxes of $N_2H^+/C^{18}O = 0.02$ and N_2H^+/CO = 0.007 given our fiducial model setup.

Ionization from the central star could also affect the target flux ratios. Increasing the stellar X-ray luminosity to 1.6×10^{32} erg s^{-1} had little effect on the flux ratios relative to the fiducial model. However, it did increase the N_2H^+/CO flux ratio to 0.04–1.8 and $N_2H^+/C^{18}O$ flux ratio to 1–800 in the cold disk model for gas-to-dust ratios of 10–100. Although the upper end of these ratios exceeds the observed values, the

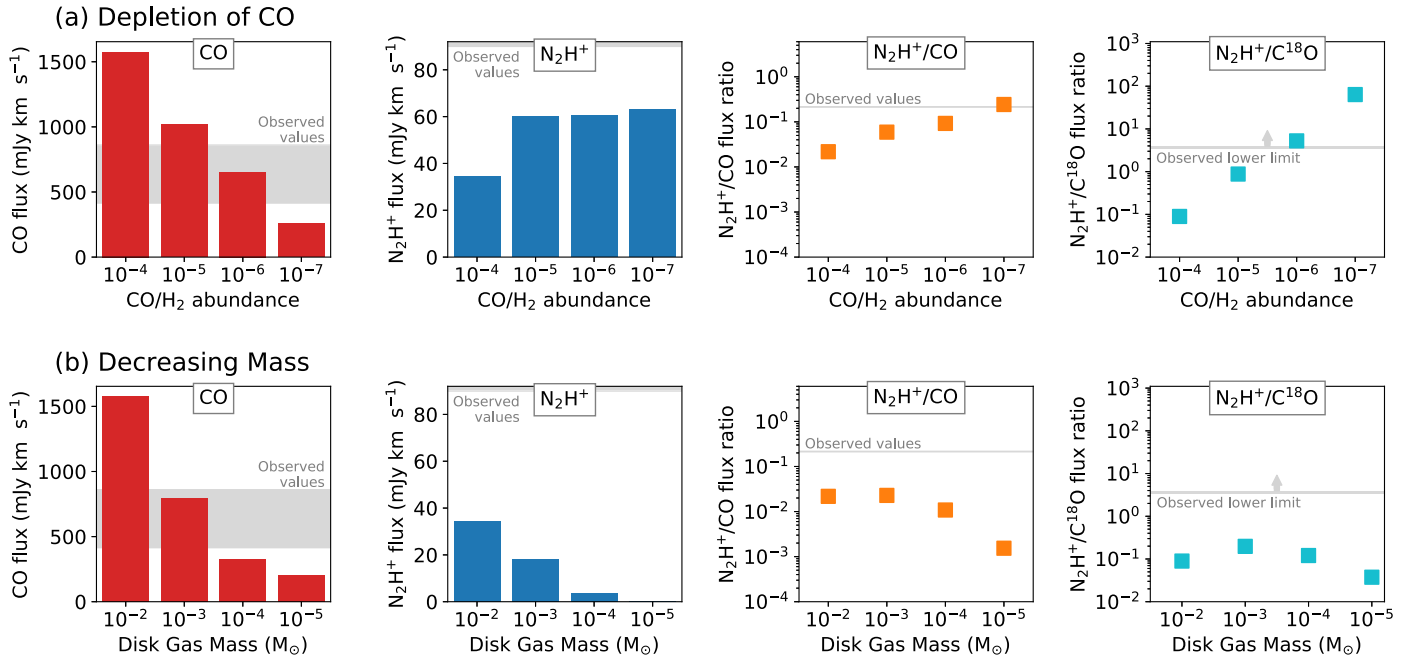

Figure 9. Calculated fluxes for our set of cold disk models. From left to right, the CO $J = 2$–1 flux, N_2H^+ $J = 3$–2 flux, ratio of the N_2H^+ $J = 3$–2 to CO $J = 2$–1 flux, and ratio of the N_2H^+ $J = 3$–2 to $C^{18}O$ $J = 2$–1 flux are plotted. Values are shown for the cold disk model with the gas mass increased by a factor of 10 (gas-to-dust mass ratio of 1000) and additional models with this gas mass where the CO/H_2 abundance ratio is lowered by factors of 10–1000× (a), and for the high mass model and additional models where the disk gas mass is lowered by factors of 10–1000× (b). The range of observed values for the Upper Sco sources are show for comparison in gray.

absolute fluxes are too low to be consistent with observations (factor of 3–20× lower). Therefore, enhanced disk ionization alone is not enough to explain the high N_2H^+/CO flux ratios in the observed Upper Sco disks.

3.3.3. Disk Size

These model results depend on the assumed disk structure including the radial extent of gas and dust. Additional versions of the fiducial model were run with outer disk radii of 50 and 200 au (Table 4). The resulting N_2H^+/CO flux ratios were 0.01 and 0.005 for the 50 and 200 au cases, respectively. This compares to 0.01 for the fiducial model with an outer disk radius of 100 au and remains far below the observed values of 0.21–0.35 in Upper Sco. $N_2H^+/C^{18}O$ flux ratios remained at about 0.04–0.05 in the models of all three sizes. N_2H^+ and CO fluxes scaled roughly with the disk size, with the exception of the $C^{18}O$ and N_2H^+ fluxes being comparable for the 100 and 200 au disks. An additional model of a more massive disk with a total gas mass of 5×10^{-2} $M_\odot$ and an outer radius of 200 au was also run. The $N_2H^+/C^{18}O$ flux ratio for the massive disk was 0.15 and N_2H^+/CO was 0.02, which are still 10× lower than the observed values. Similarly minimal changes were seen in the flux ratios for the cold disk model in these cases. Altering the disk size does not appear to significantly alter the N_2H^+/CO flux ratio in the manner necessary to explain the observations.

3.3.4. Effects of Dust Settling

The median SED for disks in Upper Sco shows that on average these older disks are more settled than a typical disk from the Taurus region (Mathews et al. 2013). To approximate increased dust settling in the models, the large dust population was constrained to a lower scale height than the small dust. The small dust was set to have a scale height of 10 au at a radius of 80 au. Values of 1, 2, 5, and 10 au were used for the scale height of the large dust to test a range relative to the extent of the small dust and illustrate the effects of large dust settling on the target flux ratios. The resulting N_2H^+/CO and $N_2H^+/C^{18}O$ flux ratios varied from each other by a factor of $\lesssim$2 and were no greater than 5× the values from the fiducial model. Although the degree of large dust settling may alter the flux ratios, changes due to this factor alone are not enough to reproduce the observed flux ratios with our models.

3.3.5. Disk Lifetime

The models presented so far were run for 1 Myr as a representative timescale. However, at longer timescales of 1–10 Myr, additional chemical reactions become important, especially the conversion of CO and N_2 into less volatile species through destruction in the gas-phase by He^+ and/or reactions with H and OH on grain surfaces. The depletion of gas-phase CO through these reactions has been studied under a wide range of physical parameters in the disk (Bosman et al. 2018; Schwarz et al. 2018). The effectiveness of these reactions depends on the disk conditions, including the level of ionization in the disk. It is possible that this chemical depletion of CO may result in the low CO abundances needed to explain the observed fluxes in the Upper Sco disks, if N_2 is impacted relatively less.

The relative depletion that occurs in the time period from 1 to 10 Myr of CO versus N_2 differs between our fiducial and cold disk models. Adopting a timescale of 10 Myr results in higher N_2H^+ and lower CO and $C^{18}O$ fluxes in the fiducial model and lower fluxes for all three in the cold disk model. The flux values and the flux ratios of interest are changed by less than a factor of 10. Given the dependency of the late-stage chemical depletion of CO on disk conditions, a more comprehensive comparison of the relative depletion of CO and N_2 and how this alters the N_2H^+/CO and $N_2H^+/C^{18}O$ flux ratios is recommended for future work.

4. Discussion

4.1. Disk Comparison

The DISCS program probed the chemical composition of a diverse set of protoplanetary disks with a series of observations by the Sumbmilliter Array in 2009–2010. The observations targeted 10 different chemical species in six Taurus sources (DM Tau, AA Tau, LkCa 15, GM Aur, CQ Tau, and MWC 480) and six Southern sky sources (IM Lup, SAO 206462, HD 142527, AS 209, AS 205, and V4046 Sgr). The DISCS sample focuses on only large, CO-bright disks, such that they would be resolvable at a few hundred au by the SMA in the compact configuration. In addition, the chosen sources could be mapped in CO and disks with contaminating emission from the parent cloud were excluded based on previous observations. A range in spectral types and bolometric luminosities, accretion rates, X-ray luminosities, and disk geometries (disks with gaps or holes versus full disks) are represented in the DISCS sample. The observed Upper Sco disks show distinct behavior in their relative N_2H^+ and CO fluxes from the entire sample, despite its diversity.

Acknowledging the uncertainties in stellar age, the majority of the sources targeted in the DISCS survey are similar or younger in age than the Upper Sco disks, which are estimated to be in the range of 5–11 Myr old (Preibisch et al. 2002; Pecaut et al. 2012). A portion of the DISCS disks are considered (pre-)transitional and show evidence of disk clearing via gaps or inner holes in their structures. J160823–193001 and J160900–190852 are not known to be transitional disks. Even so, the low dust masses and weak-CO emission seen in the Upper Sco population are taken to be signs of disk evolution indicating a progression toward transitional or debris-disk stages relative to disks from younger star-forming regions (Ansdell et al. 2017). A rough age comparison is shown for T Tauri sources in Figure 3 based on values from the following sources: Kraus & Hillenbrand (2009), Andrews et al. (2010), Mawet et al. (2012), Miret-Roig et al. (2018), and Sokal et al. (2018).

Because CO depletion has been proposed to be a time-dependent process (e.g., Favre et al. 2013), if N_2H^+/CO flux ratios are tracking CO depletion as predicted, and CO depletion increases over time, we would expect to see larger N_2H^+/CO flux ratios for older sources. In the middle panel of Figure 3, we do not see a clear trend in the N_2H^+/CO flux ratios with stellar age. In particular, V4046 Sgr is part of the β Pictoris moving group with an estimated age of 13^{+7}_{-0} Myr (Miret-Roig et al. 2018) and therefore older than our Upper Sco targets, but has a lower value. However, this may be an effect caused by optically thick $^{12}C^{16}O$ emission and the circumbinary nature of the disk. In fact, the $N_2H^+/C^{18}O$ flux ratios do hint at a trend with age where the older disks (V4046 Sgr, TW Hya, and J160900–190852) have higher values than the younger disks (Figure 3, bottom panel).

HD 163296 and MWC 480 do not fit within this trend, but they are also the only disks around Herbig Ae/Be stars in the sample with $C^{18}O$ measurements. We can therefore conclude that some environmental factors, such as the spectral type of the central star and its impact on the disk thermal structure, are likely important for determining the observed flux ratios and that further measurements are needed to investigate these potential trends with source parameters. Ultimately, given that the disks in Upper Sco differ in multiple ways from the other observed disks, having fainter CO and continuum fluxes and perhaps smaller sizes as well as advanced age, the primary cause of the differences in flux ratios is not yet clear.

Based on HD measurements, TW Hya, GM Aur, and DM Tau are found to have CO/H_2 ratios lower than interstellar by up to 5–100× (Bergin et al. 2013; McClure et al. 2016). Despite the observed CO depletion, these disks do not show enhanced N_2H^+/CO fluxes relative to the other DISCS sample targets. This again may be a result of the likely optically thick $^{12}C^{16}O$ emission in these large disks, preventing accurate comparisons of the N_2H^+/CO column densities based on flux. For TW Hya, where $C^{18}O$ emission is available, the $N_2H^+/C^{18}O$ flux does appear relatively high compared to other sources, the younger sources in particular (Figure 3).

4.2. Connections to Solar System N and C Elemental Ratios

Bergin et al. (2015) highlights the low nitrogen-to-carbon ratios of bodies in our solar system. In the case of the Earth, complex processes occurring at various stages of planet formation including differentiation, metamorphism, atmospheric loss, and late delivery of materials can affect the final composition. However, the amount of processing is more limited for primitive meteorites and comets, placing a larger emphasis on accretion of materials and processing occurring within the protoplanetary disk. Observations of comets have found N_2/CO ratios below the solar nebula value of 0.15, ranging from a comparable value of $N_2/CO \sim 0.08$ for comet C/2016 R2 to the highly depleted value of $<6 \times 10^{-5}$ in Hale–Bopp (Cochran et al. 2000; Biver et al. 2018). An in situ measurement by ROSINA, the mass spectrometer on board the *Rosetta* spacecraft, determined a N_2/CO ratio of 5.7×10^{-3} for comet 67P/Churyumov–Gerasimenko (Rubin et al. 2015). This is ∼25× below the estimated value for the solar nebula.

Photodesorption of mixed layered ices can result in the enhanced release of some chemical species relative to others. Bertin et al. (2013) consider the scenario where N_2 condenses at a slightly lower temperature (2 K less) than CO and deposits as a thin layer of N_2 on top of an existing CO-rich ice. This results in decreased CO and increased N_2 photodesorption rates according to their laboratory experiments. They propose this scenario as an explanation for nitrogen-enriched gas in dense cores where N_2 depletion onto grains appears to occur at higher densities than for CO (Bergin et al. 2002; Pagani et al. 2005, 2012). Such a mechanism could release enhanced levels of nitrogen into the gas while CO remains frozen onto grain surfaces and becomes incorporated into forming planestimals with a greater efficiency. Such a scenario is consistent with both the low nitrogen content relative to carbon in primitive solar system bodies in addition to the high N_2H^+/CO fluxes observed in the Upper Sco disks. This correlation may indicate that similar chemical evolution of the gas occurred in the solar nebula and the Upper Sco disks.

5. Conclusion

Here we present the detection of $N_2H^+ J = 3$–2 emission in two disks in the Upper Scorpius region. Ionized H_2 gas is necessary for the main N_2H^+ production reaction, therefore revealing these disks to still be rich in primordial gas at their age of ∼5–11 Myr. Previous ALMA observations found disks in Upper Sco to have weaker CO and continuum emission relative to younger star-forming regions, presumably as a result of disk evolution (Barenfeld et al. 2016, 2017; Ansdell et al. 2017). The two disks observed here have higher N_2H^+/CO flux ratios than previously observed CO-bright disks. This may be the result of disk evolution, indicating different chemical and/or physical pathways for nitrogen- and carbon-bearing

species. Line fluxes predicted by the thermochemical model show that enhanced N_2H^+/CO emission can be explained by selective CO depletion relative to H_2. The resulting high nitrogen-to-carbon content in the gas would correspond to low nitrogen-to-carbon ratios in solids forming in the disk, consistent with trends in elemental abundances of meteorites and comets in our solar system compared to the Sun (Bergin et al. 2015). This connection may hint at similar evolutionary pathways existing in the Upper Sco disks and the solar nebula.

Our basic set of thermochemical disk models show that low CO fluxes can be achieved via total gas depletion or selective depletion of CO, but the N_2H^+ fluxes of the observed Upper Sco disks can only be explained by relatively high disk gas masses in combination with removal of CO. Without the additional constraints provided by N_2H^+, the disk gas mass would be severely underpredicted in the case of CO depletion. However, time-dependent loss of CO via disk evolution similar to that proposed in TW Hya may not be the only explanation for the enhanced N_2H^+/CO flux ratios. Individual disk environments including initial gas composition, ionization, temperature structure, and timescales of disk evolution may also influence these flux ratios. Further study of a larger sample of disks is required to constrain the effects of these additional parameters. Disks that are suspected to be CO-depleted based on comparisons of CO measurements to other indicators of the total disk mass may be particularly interesting targets for N_2H^+ follow-up observations. Regardless, the N_2H^+ observations here indicate that the bright protoplanetary disks often targeted for observational studies are not fully representative of the ~5–11 Myr old, weak-CO-emitting disks in Upper Sco. The gas chemistry (and/or physical structure) of these Upper Sco disks differs in an observable way due to their disk conditions and/or evolutionary stage.

The investigation of volatile species beyond CO is crucial for understanding how disks evolve chemically and physically. This is particularly true if CO depletion is a widespread phenomenon among disk populations even at young ages. N_2H^+ provides additional information regarding the disk composition and/or physical structure and warrants further investigation.

This material is based upon work supported by the National Science Foundation Graduate Research Fellowship under grant No. DGE-1144469 and funding from NSF grants AST-1514670 and AST-1344133 (INSPIRE) as well as NASA NNX 16AB48G. J.C. acknowledges support from the National Aeronautics and Space Administration under grant No. 15XRP15_20140 issued through the Exoplanets Research Program. K.Z. acknowledges the support of NASA through Hubble Fellowship grant HST-HF2-51401.001-A. J.H. acknowledges support from the National Science Foundation Graduate Research Fellowship under grant No. DGE-1144152. This work makes use of the following ALMA data: ADS/JAO.ALMA#2015.1.01199.S, ADS/JAO.ALMA#2011.0.00526.S, ADS/JAO.ALMA#2015.1.00964.S, and ADS/JAO.ALMA#2013.1.00226.S. ALMA is a partnership of ESO (representing its member states), NSF (USA) and NINS (Japan), together with NRC (Canada), MOST and ASIAA (Taiwan), and KASI (Republic of Korea), in cooperation with the Republic of Chile. The Joint ALMA Observatory is operated by ESO, AUI/NRAO, and NAOJ. The National Radio Astronomy Observatory is a facility of the National Science Foundation operated under cooperative agreement by Associated Universities, Inc. We thank NRAO for assistance with data reduction and the anonymous reviewer for critically reading the manuscript and providing insightful feedback.

Software: APLpy (Robitaille & Bressert 2012), Astropy (Astropy Collaboration 2013, 2018), CASA (McMullin et al. 2007), Matplotlib (Hunter 2007).

Appendix

Figure 10 shows the moment 1 maps of N_2H^+ and CO emission from the observed Upper Sco disks.

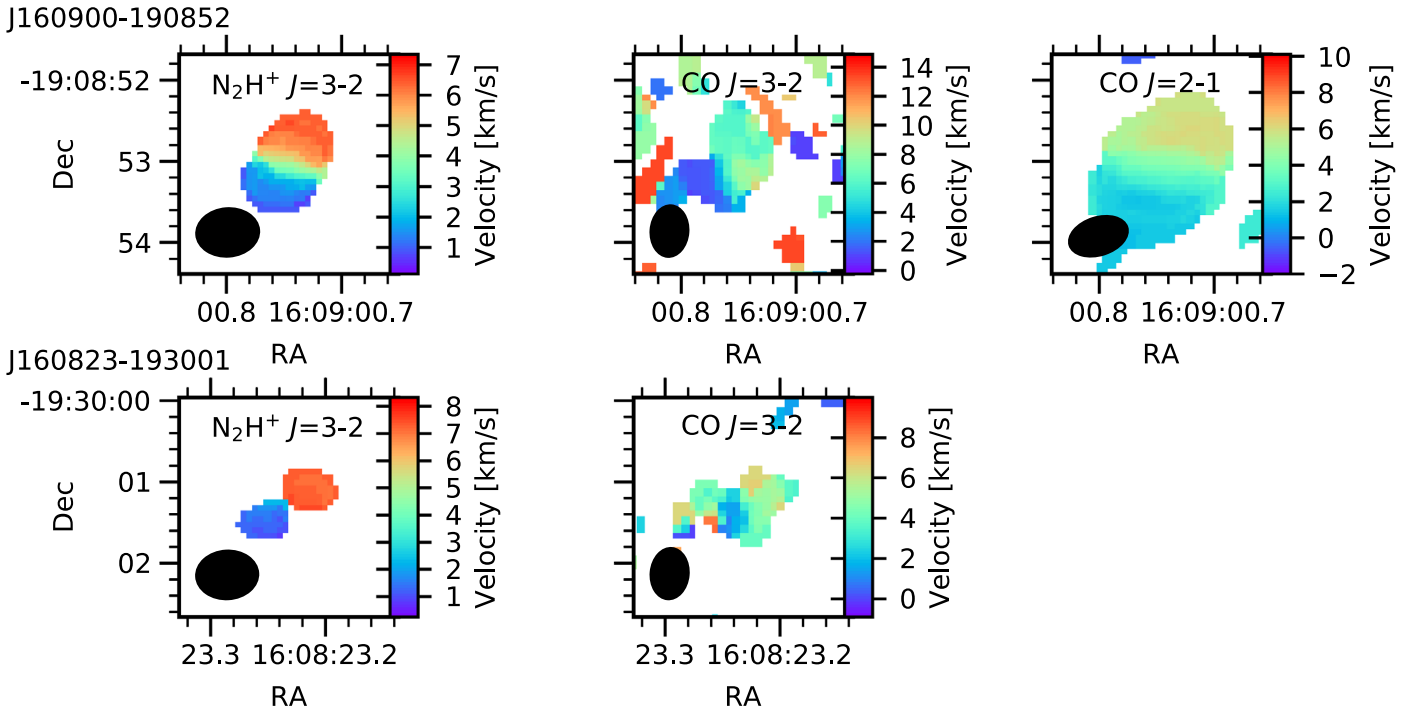

Figure 10. Moment 1 maps of N_2H^+ and CO emission from the Upper Sco disks J160900–190852 (top row) and J160823–193001 (bottom row).

ORCID iDs

Dana E. Anderson https://orcid.org/0000-0002-8310-0554
Geoffrey A. Blake https://orcid.org/0000-0003-0787-1610
Edwin A. Bergin https://orcid.org/0000-0003-4179-6394
Ke Zhang https://orcid.org/0000-0002-0661-7517
John M. Carpenter https://orcid.org/0000-0003-2251-0602
Kamber R. Schwarz https://orcid.org/0000-0002-6429-9457
Jane Huang https://orcid.org/0000-0001-6947-6072
Karin I. Öberg https://orcid.org/0000-0001-8798-1347

References

Aikawa, Y., Furuya, K., Nomura, H., et al. 2015, ApJ, 807, 120
Alexander, R., Pascucci, I., Andrews, S., Armitage, P., & Cieza, L. 2014, in Protostars and Planets VI, ed. H. Beuther et al. (Tucson, AZ: Univ. Arizona Press), 475
Andrews, S. M., Wilner, D. J., Hughes, A. M., et al. 2012, ApJ, 744, 162
Andrews, S. M., Wilner, D. J., Hughes, A. M., Qi, C., & Dullemond, C. P. 2010, ApJ, 723, 1241
Ansdell, M., Williams, J. P., Manara, C. F., et al. 2017, AJ, 153, 240
Ansdell, M., Williams, J. P., van der Marel, N., et al. 2016, ApJ, 828, 46
Astropy Collaboration, Price-Whelan, A. M., Sipőcz, B. M., et al. 2018, AJ, 156, 123
Astropy Collaboration, Robitaille, T. P., Tollerud, E. J., et al. 2013, A&A, 558, A33
Barenfeld, S. A., Carpenter, J. M., Ricci, L., & Isella, A. 2016, ApJ, 827, 142
Barenfeld, S. A., Carpenter, J. M., Sargent, A. I., Isella, A., & Ricci, L. 2017, ApJ, 851, 85
Bergin, E. A., Alves, J., Huard, T., & Lada, C. J. 2002, ApJL, 570, L101
Bergin, E. A., Blake, G. A., Ciesla, F., Hirschmann, M. M., & Li, J. 2015, PNAS, 112, 8965
Bergin, E. A., Cleeves, L. I., Crockett, N., & Blake, G. A. 2014, FaDi, 168, 61
Bergin, E. A., Cleeves, L. I., Gorti, U., et al. 2013, Natur, 493, 644
Bertin, M., Fayolle, E. C., Romanzin, C., et al. 2013, ApJ, 779, 120
Bisschop, S. E., Fraser, H. J., Öberg, K. I., van Dishoeck, E. F., & Schlemmer, S. 2006, A&A, 449, 1297
Biver, N., Bockelée-Morvan, D., Paubert, G., et al. 2018, A&A, 619, A127
Bosman, A. D., Walsh, C., & van Dishoeck, E. F. 2018, A&A, 618, A182
Carpenter, J. M., Ricci, L., & Isella, A. 2014, ApJ, 787, 42
Cleeves, L. I., Bergin, E. A., Qi, C., Adams, F. C., & Öberg, K. I. 2015, ApJ, 799, 204
Cleeves, L. I., Öberg, K. I., Wilner, D. J., et al. 2016, ApJ, 832, 110
Cochran, A. L., Cochran, W. D., & Barker, E. S. 2000, Icar, 146, 583
Du, F., & Bergin, E. A. 2014, ApJ, 792, 2
Favre, C., Cleeves, L. I., Bergin, E. A., Qi, C., & Blake, G. A. 2013, ApJL, 776, L38
Fayolle, E. C., Balfe, J., Loomis, R., et al. 2016, ApJL, 816, L28
Fray, N., Bardyn, A., Cottin, H., et al. 2017, MNRAS, 469, S506
Gaia Collaboration, Brown, A. G. A., Vallenari, A., et al. 2018, A&A, 616, A1
Gorti, U., Dullemond, C. P., & Hollenbach, D. 2009, ApJ, 705, 1237
Guilloteau, S., Reboussin, L., Dutrey, A., et al. 2016, A&A, 592, A124
Heays, A. N., Visser, R., Gredel, R., et al. 2014, A&A, 562, A61
Heritier, K. L., Altwegg, K., Balsiger, H., et al. 2017, MNRAS, 469, S427
Huang, J., Andrews, S. M., Cleeves, L. I., et al. 2018, ApJ, 852, 122
Huang, J., Öberg, K. I., & Andrews, S. M. 2016, ApJL, 823, L18
Huang, J., Öberg, K. I., Qi, C., et al. 2017, ApJ, 835, 231
Hunter, J. D. 2007, CSE, 9, 90
Kastner, J. H., Qi, C., Dickson-Vandervelde, D. A., et al. 2018, ApJ, 863, 106
Kraus, A. L., & Hillenbrand, L. A. 2009, ApJ, 704, 531
Krijt, S., Schwarz, K. R., Bergin, E. A., & Ciesla, F. J. 2018, ApJ, 864, 78
Lee, E. J., & Chiang, E. 2016, ApJ, 817, 90
Long, F., Herczeg, G. J., Pascucci, I., et al. 2017, ApJ, 844, 99
Mathews, G. S., Pinte, C., Duchêne, G., Williams, J. P., & Ménard, F. 2013, A&A, 558, A66
Mathis, J. S. 1990, ARA&A, 28, 37
Mawet, D., Absil, O., Montagnier, G., et al. 2012, A&A, 544, A131
McClure, M. K., Bergin, E. A., Cleeves, L. I., et al. 2016, ApJ, 831, 167
McMullin, J. P., Waters, B., Schiebel, D., Young, W., & Golap, K. 2007, adass XVI, 376, 127
Miotello, A., Bruderer, S., & van Dishoeck, E. F. 2014, A&A, 572, A96
Miret-Roig, N., Antoja, T., Romero-Gómez, M., & Figueras, F. 2018, A&A, 615, A51
Öberg, K. I., Qi, C., Fogel, J. K. J., et al. 2010, ApJ, 720, 480
Öberg, K. I., Qi, C., Fogel, J. K. J., et al. 2011, ApJ, 734, 98
Pagani, L., Bourgoin, A., & Lique, F. 2012, A&A, 548, L4
Pagani, L., Pardo, J.-R., Apponi, A. J., Bacmann, A., & Cabrit, S. 2005, A&A, 429, 181
Pascucci, I., Sterzik, M., Alexander, R. D., et al. 2011, ApJ, 736, 13
Pecaut, M. J., Mamajek, E. E., & Bubar, E. J. 2012, ApJ, 746, 154
Pollack, J. B., Hubickyj, O., Bodenheimer, P., et al. 1996, Icar, 124, 62
Preibisch, T., Brown, A. G. A., Bridges, T., Guenther, E., & Zinnecker, H. 2002, AJ, 124, 404
Qi, C., Öberg, K. I., Andrews, S. M., et al. 2015, ApJ, 813, 128
Qi, C., Öberg, K. I., & Wilner, D. J. 2013a, ApJ, 765, 34
Qi, C., Öberg, K. I., Wilner, D. J., et al. 2013b, Sci, 341, 630
Reboussin, L., Wakelam, V., Guilloteau, S., Hersant, F., & Dutrey, A. 2015, A&A, 579, A82
Robitaille, T., & Bressert, E. 2012, APLpy: Astronomical Plotting Library in Python, Astrophysics Source Code Library, ascl:1208.017
Rosenfeld, K. A., Andrews, S. M., Hughes, A. M., Wilner, D. J., & Qi, C. 2013, ApJ, 774, 16
Rosenfeld, K. A., Qi, C., Andrews, S. M., et al. 2012, ApJ, 757, 129
Rubin, M., Altwegg, K., Balsiger, H., et al. 2015, Sci, 348, 232
Schwarz, K. R., & Bergin, E. A. 2014, ApJ, 797, 113
Schwarz, K. R., Bergin, E. A., Cleeves, L. I., et al. 2016, ApJ, 823, 91
Schwarz, K. R., Bergin, E. A., Cleeves, L. I., et al. 2018, ApJ, 856, 85
Sokal, K. R., Deen, C. P., Mace, G. N., et al. 2018, ApJ, 853, 120
van 't Hoff, M. L. R., Walsh, C., Kama, M., et al. 2017, A&A, 599, A101
Visser, R., van Dishoeck, E. F., & Black, J. H. 2009, A&A, 503, 323
Weidenschilling, S. J., & Cuzzi, J. N. 1993, in Protostars and Planets III, ed. E. H. Levy & J. I. Lunine (Tucson, AZ: Univ. Arizona Press), 1031
Wyatt, M. C. 2008, ARA&A, 46, 339
Youdin, A. N., & Goodman, J. 2005, ApJ, 620, 459
Yu, M., Willacy, K., Dodson-Robinson, S. E., Turner, N. J., & Evans, N. J., II 2016, ApJ, 822, 53
Zhang, K., Bergin, E. A., Blake, G. A., Cleeves, L. I., & Schwarz, K. R. 2017, NatAs, 1, 130
Zhang, K., Isella, A., Carpenter, J. M., & Blake, G. A. 2014, ApJ, 791, 42